2018B1167 BL20XU

高分解能・高エネルギーX 線位相コントラスト法と構造材料への応用
High-Resolution / High-Energy X-ray Phase-Contrast Tomography Techniques and their Application to Structural Metals

平山 恭介 [a,b], 戸田 裕之 [a], 蘇 航 [a], 岡村 海 [a], 鈴木 芳生 [c], 竹内 晃久 [d], 上椙 真之 [d], 清水 一行 [a,e]

Kyosuke Hirayama[a,b], Hiroyuki Toda[a], Han Su[a], Kai Okamura[a], Yoshio Suzuki[c], Akihisa Takeuchi[d], Masayuki Uesugi[d] and Kazuyuki Shimizu[a,e]

[a] 九州大学, [b] 京都大学, [c] 高エネルギー加速器研究機構, [d] 高輝度光科学研究センター, [e] 岩手大学

[a]Kyushu University, [b]Kyoto University, [c] High Energy Accelerator Research Organization, [d] Japan Synchrotron Radiation Research Institute, [e]Iwate University

Abstract

Three high-resolution / high-energy phase-contrast X-ray nano-tomography (XNT) techniques were tested, with the spatial resolution, contrast, and artefacts being evaluated. All the experiments utilized apodization Fresnel zone plates (A-FZP), which have been recently developed for the purpose of imaging characteristics improvement, taking advantage of the A-FZP's secondary benefit that its thicker inner zone makes it readily applicable for use with high X-ray energies. The techniques employed in the present study were the imaging-type XNT combined with Zernike phase-contrast optics, the X-ray schlieren phase-contrast method, and the defocusing phase-contrast method. All the methods successfully recognized a density difference of 3.7 % between α and β grains in a Ti-6Al-4V alloy at an X-ray energy of 20 keV, together with an excellent spatial resolution within a scanning time of 1h. The Zernike phase-contrast method was then successfully applied to in-situ XNT observation of the transformation behavior of retained austenite in a duplex carbon steel at an X-ray energy of 20 ~ 37.7 keV. The characteristic local transformation behavior of the retained austenite was revealed through a series of 3D images and quantitative data obtained from the 3D images.

Keywords: Phase-contrast imaging, X-ray tomography, Schlieren phase-contrast method, Zernike phase-contrast method, Austenite steel, Titanium alloy

1 Introduction：

Various visualization techniques, such as those of scanning and transmission electron microscopy, have been widely used in materials science and engineering. However, such observations are fundamentally two dimensional (hereinafter 2D) and made on a surface or thin film, meaning that their validity as representations of internal microscopic features is often not assured. High-resolution X-ray tomography techniques would appear to offer a useful alternative tool for three dimensional (hereinafter 3D) observation of the internal microstructural features of structural metals. Ordinary projection-type X-ray microtomography (hereinafter XMT) readily provides approximately 1 μm in spatial resolution [1], while full-field X-ray microscopy, an imaging-type X-ray nanotomography (hereinafter XNT) technique, enables spatial resolution enhancement by more than one order of magnitude [2].

In-situ testing on an XMT and XNT rotation stage can provide a temporal sequence of 3D images, a type of periodic 3D observation referred to as 4D observation. 4D XMT and XNT observations are a robust tool for investigating various internal time-evolution behaviors occurring in the bulk of a material. However, information on the process and chronology of such behavior is either simply not obtained with conventional 2D techniques, or unrepresentative of the processes that occur in the interior of actual structural materials.

In the ordinary absorption-contrast XMT, the 3D distribution of linear absorption coefficients is reconstructed from 2D projections [3]. Since the secondary particles or precipitates embedded in alloys are essentially intermetallic compounds among alloying elements and an underlying metal matrix, microstructural features are often "transparent" (i.e. poor contrast to distinguish two microstructures) with respect to the matrix in the case of the absorption-contrast XMT. The ratio of real (δ) to imaginary (β) elements (representing the phase shift and absorption, respectively) of a complex refractive index, δ/β, reaches more than 10 for structural metals at X-ray energies higher than 10 keV [4]. It would be of significant value if all the internal microstructural features could be clearly visualized in 3D at a reasonably high magnification, utilizing such phase shift.

Three different types of technique have thus far been developed for achieving such high-resolution and

high-contrast XMT and XNT in structural metals [5 ~ 9]. The first one is a combination of Kirkpatrick–Baez (hereinafter KB) mirror optics for magnified synchrotron XNT and an X-ray holotomography technique. The second one is a lab-based XNT system in which a flat X-ray lens called a Fresnel zone plate (hereinafter FZP) is combined with Zernike phase-contrast optics. The third one is the differential phase-contrast (hereinafter DPC) tomography technique.

The X-ray energy range for a FZP is limited by its zone thickness, which is in the trade-off relationship with the spatial resolution [2]. High-resolution FZP requires an outermost zone width of tens to 100 nm and high X-ray energy imaging requires its sufficient thickness, implying that a high aspect ratio of at least several tens is needed in the case of high X-ray energy [2]. Since presently available ordinary FZPs provide at most an aspect ratio of 10 or less, thickness is limited to 1 μm. The available X-ray energy range for FZP-based XNT has therefore been limited to 10 keV or less [2, 8, 9, 10], meaning that samples of hair-like thinness must be used, which may be unrepresentative of the bulk of the given material.

In sum, the difficulties involved in in-situ 4D XNT observation of metallic samples, with reasonably high contrast and resolution, have remained intractable due to the existence of hitherto insuperable problems.

Most recently, however, there has been technological innovation in FZP development. Takeuchi et al., for example, have developed a special FZP, called an apodization FZP (hereinafter A-FZP) [11], which incorporates a Gaussian beam optical system in the optical configuration of an XNT system, thereby improving imaging characteristics, which enables more quantitative and sensitive XNT measurement [11]. The zone depth is uniform in the case of a conventional FZP; whereas, in an A-FZP, the zone depth gradually decreases toward the outermost zone, where a high aspect ratio is required in the case of the conventional FZP, yielding the secondary benefit that A-FZPs with thicker inner zones are readily applicable for use with high X-ray energies.

In the present study, three high-resolution / high-energy phase-contrast XNT techniques were tested, with A-FZPs as the objective lens for better spatial resolution at higher X-ray energies. These included the imaging-type XNT combined with Zernike phase-contrast optics, the X-ray schlieren phase-contrast method, and the defocusing phase-contrast method, which was tested using the same experimental set-up as in the schlieren phase-contrast method. The X-ray schlieren phase-contrast method was introduced in 1959 in the text book of Born and Wolf [12]. In the hard X-ray region, schlieren-like contrast have already been achieved using crystal analyzer optics by Goetz et al. [13]. However, the schlieren imaging with lens optics has not been attempted in the X-ray region. To the best of the present authors' knowledge, since then there has been only one published report on the application of this method to the tomography technique, in which Watanabe et al. [14].

A selected technique was then applied to the in-situ 4D XNT observation of a duplex steel with limited density difference between the two microstructures, and the advantages and disadvantages of the selected technique will be discussed from the viewpoint of practical applications.

2 Experimental：

XMT and XNT experiments were performed at beam line BL20XU of SPring-8 [15]. A monochromatic X-ray beam of 20 keV was produced by a liquid nitrogen-cooled Si (111) double crystal monochromator, with 30 keV being subsequently used for a limited number of trials at a higher X-ray energy. Fundamentally needle-like still specimens were used as idealized samples, which were mounted on a rotational stage located approximately 80 m from the X-ray source. In the latter half of the study, a miniature material test rig was mounted on the rotational stage to load a tensile specimen. XMT and XNT set-ups were assembled at the same time in BL20XU, enabling the use of imaging techniques with different levels of spatial resolution for a single specimen [16]. The imaging set-ups were switched within a few minutes by remotely advancing and withdrawing a CMOS camera and several optical devices to and from an optical axis. The entire specimen was imaged using the projection-type XMT technique to determine a region of interest embedded in a specimen, and then the imaging-type XNT technique was employed at a higher magnification to observe the region of interest. The conventional filtered backprojection algorithm was employed to reconstruct image slices for both the absorption-contrast and phase-contrast images [17]. The spatial resolution was quantitatively evaluated between the two microstructures in the reconstructed slices.

2.1 X-ray nanotomography experiments

2.1.1 Imaging-type XNT in Zernike phase-contrast mode

The experimental set-ups for the imaging-type XNT are shown in Figs. 1 (a) and (b). Köhler illumination [2] with a rotating condenser zone plate was used for the imaging-type XNT with Zernike phase-contrast mode, as shown in Fig. 1 (a). An annular aperture was placed in front of the condenser zone plate. An A-FZP of 310 μm in diameter and 100 nm in outermost zone width was used. The A-FZPs were fabricated, by NTT Advanced Technology Corp., by patterning a 2-μm thick tantalum layer on a transparent membrane of 2-μm

thick Ru / SiC / SiN, using the electron beam lithography technique. The focal length of the A-FZP was 500 mm at 20 keV, and the diffraction efficiency was 9.1 % at 20 keV. The A-FZP was located 500 mm downstream from the sample, and an annular phase plate was placed at the back focal plane of the objective A-FZP (i.e., 500 mm from the A-FZP), thereby providing the phase shift necessary for the Zernike phase-contrast X-ray microscope [18].

The second X-ray image detector with a CMOS (complementary metal-oxide semiconductor) camera (ORCA Flush 4.0, Hamamatsu Photonics K. K.) was set at an L of 165 m downstream from the sample, in the second experimental hutch, in a separate building from the SPring-8 Main Ring Building. Again, a combination of objective lens and 20-μm thick P43 (Gd2O2S:Tb+) powder scintillator was used. The imaging-type XNT technique with Zernike phase-contrast mode provided isotropic voxels with 0.087 μm edges. A total of 1,800 projection images were captured to reconstruct a single 3D image. The exposure time was 0.7 and 2.0 sec for a Fe-0.1C-5Mn-1Si and Ti-6Al-4V alloy, respectively.

2.1.2 Imaging-type XNT with schlieren optics

A quasi-parallel beam was employed as the illumination. A slit blade was placed horizontally immediately in front of the sample (Fig. 1 (b)) to eliminate the undesired diffraction orders of the A-FZP. A knife edge was placed at the back focal plane of the objective A-FZP, which is identical to the Zernike phase-contrast XNT experiment. The second x-ray image detector, located in the second experimental hutch, was also used for this imaging. A combination of objective lens and 20-μm thick P43 (Gd2O2S:Tb+) powder scintillator was used. A total of 1,800 projection images were captured to reconstruct a single 3D image, with isotropic voxels with 0.060 μm edges being provided in the reconstructed slices. The exposure time was 1 sec. An additional trial, the phase-contrast simply by defocusing, was performed by merely removing the knife edge from the experimental set-up shown in Fig. 1 (b) with transferring the FZP along the optical axis by 5 mm for defocusing purpose.

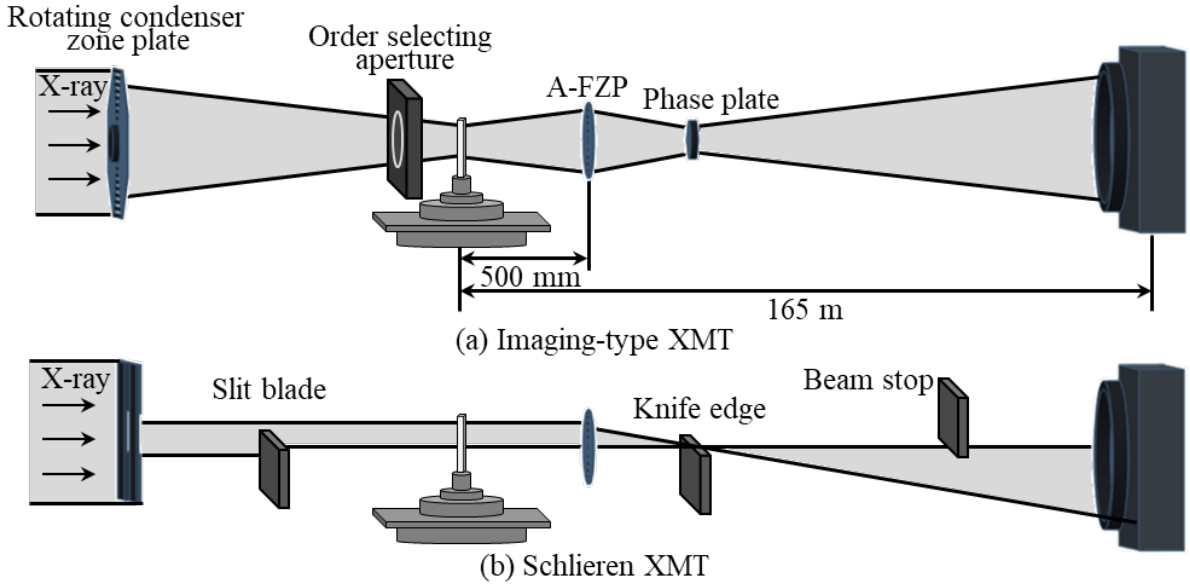

Fig. 1 Experimental set-up for (a) the imaging-type X-ray nanotomography combined with Zernike phase-contrast optics, and (b) the X-ray schlieren phase-contrast method.

2.2 Samples

A Ti-6Al-4V alloy was used for the first screening experiment due to its characteristic microstructural features; wrought Ti-6Al-4V alloy has a majority of α grain plus a minor amount of plate-like β grain distributed finely in α + β regions, as shown in Fig. 2 (a). A commercial wrought billet was hot rolled at 1073 K at a rolling reduction of 50 %, and then heat-treated at 1173 K for 96 h before furnace cooling. After thermomechanical processing, the Ti-6Al-4V exhibited a typical bimodal microstructure with a volume fraction of 60 % primary α grain of approximately 23 μm in diameter, embedded in a lamellar α + β matrix. The theoretical density values for the HCP α and BCC β grains are 4.51 and 4.35 g/cm^3, respectively [19]. A tapered needle was prepared by mechanical polishing.

A Fe-0.1C-5Mn-1Si duplex carbon steel consisting of the ferrite matrix and metastable retained austenite (Fig. 2 (b)) was used for the subsequent in-situ 4D XNT observation. This steel is unique in that the retained austenite, which has a lesser density difference from the matrix than that of the Ti-6Al-4V alloy, gradually

disappears upon loading. The density values for the ferrite and austenite grains are 7.71 and 7.65 g/cm^3, respectively.

The miniature material test rig shown in Fig. 3 (a) was positioned on a sample rotational stage, and a tensile specimen (as in Fig. 3 (b)) was machined using the electric discharge machining technique in water. Fig. 3 (c) shows the tensile nominal stress-nominal strain curve recorded during the in-situ tensile test performed under X-ray irradiation. A cylindrical region of interest of 55 μm in diameter was observed with a selected imaging-type XNT technique, at the applied load levels indicated in Fig. 3 (c), while maintaining applied displacements.

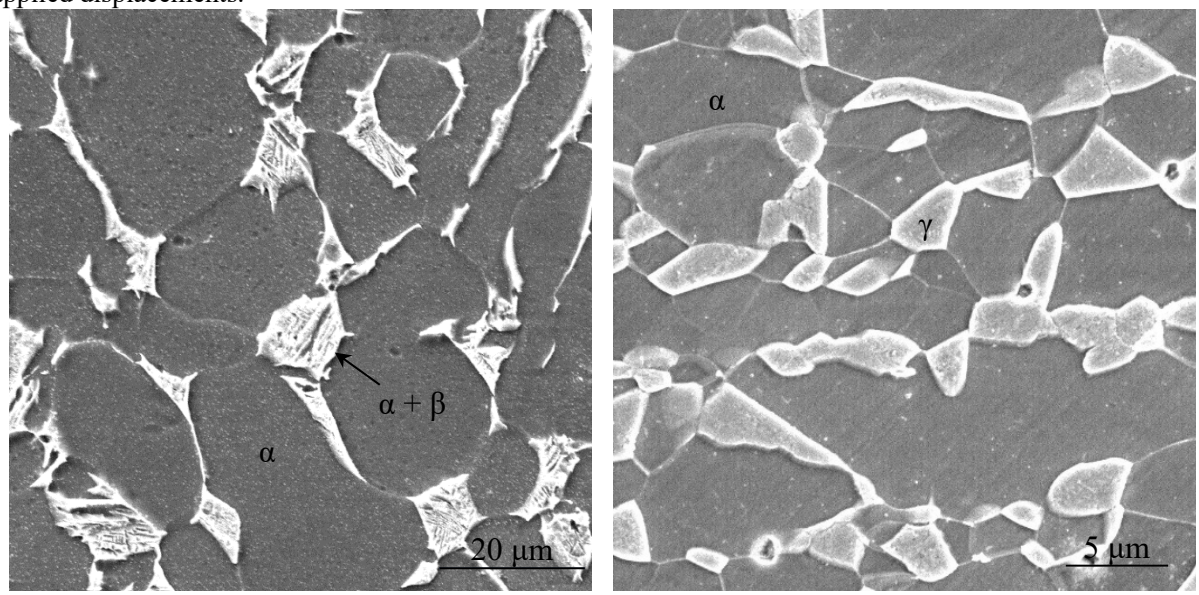

(a) Ti-6Al-4V alloy (b) Fe-0.1C-5Mn-1Si carbon steel

Fig. 2 SEM micrographs of the two model materials used in the study: (a) wrought Ti-6Al-4V alloy with a bimodal microstructure of the primary α grain and lamellar α + β matrix, and (b) Fe-0.1C-5Mn-1Si duplex carbon steel consisting of the ferrite matrix and a metastable retained austenite grain.

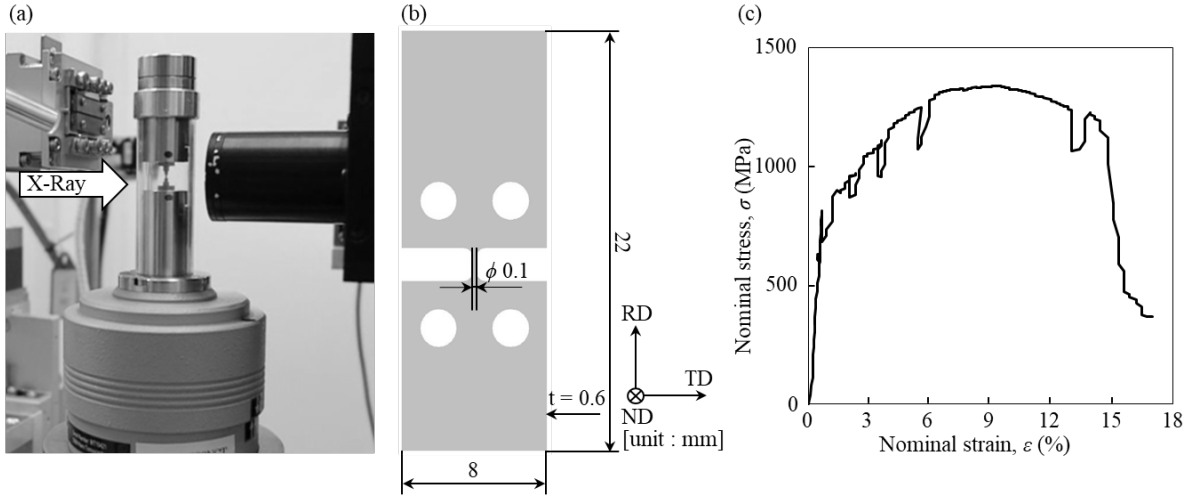

Fig. 3 (a) The miniature material test rig employed for the in-situ tensile test under X-ray irradiation. (b) A tensile specimen for the in-situ tensile test performed under X-ray irradiation, which was machined using the electric discharge machining technique. (c) A tensile nominal stress-nominal strain curve of Fe-0.1C-5Mn-1Si duplex carbon steel recorded during the in-situ tensile test performed under X-ray irradiation.

3. Comparison of the three phase-contrast XNT techniques：

Figure 4 shows virtual cross-sections of the Ti-Al-4V alloy, obtained using the three studied phase-contrast XNT techniques. Note that an edge-enhanced bright-dark image contrast is seen in Fig. 4 (b) by positioning the knife-edge at - 2 μm from the central spot. A complete dark field image, which consists only of α / β boundaries as bright lines, is also obtainable by covering the central spot with the knife-edge. However, as

this may cause degradation in the signal-to-noise ratio, due to low signal intensity, this imaging mode was not adopted in this study.

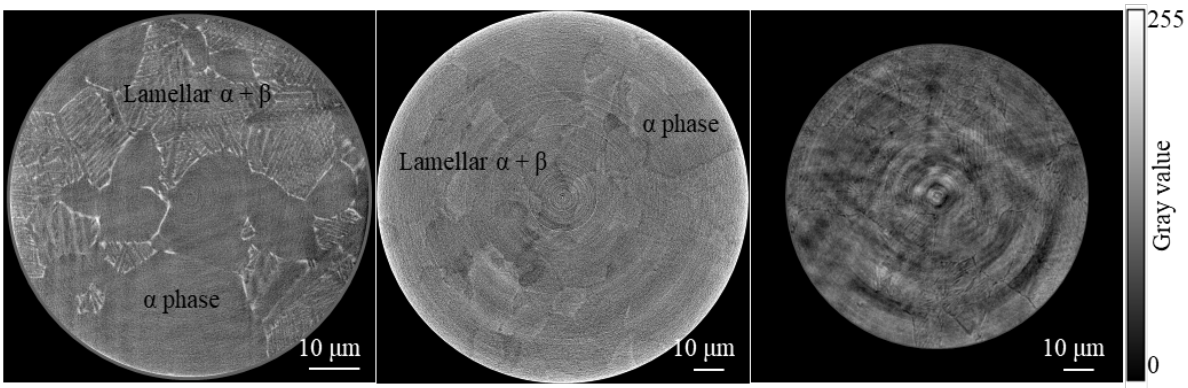

(a) Zernike phase-contrast image (b) Schlieren phase-contrast image (c) Defocusing phase-contrast image

Fig. 4 Typical virtual cross-sections of the Ti-6Al-4V alloy obtained with the three phase-contrast X-ray nanotomography techniques.

Another feature to note is the existence of the halo effect [20], which is one of the typical artefacts in Zernike phase-contrast microscopy. It is in general understood that the point spread function of an X-ray traveling through the phase plate has side lobes with amplitudes comparable to that of the main lobe [20]. The side lobe in the phase response forms a bright fringe around a dark phase [20]. In Fig. 4 (a), the darker α grain appears to be surrounded by bright narrow slips, by which the spatial resolution is degraded. The contrast of the β in the α + β lamella region is per contra enhanced by the formation of halos. There is also a general limitation on the spatial resolution in the defocusing method due to image blurring, as is seen in Fig. 4 (c) in the broadening of the α / β boundaries.

In terms of the contrast between the two microstructures, the α and α + β lamella regions are separated in the case of the schlieren phase-contrast method, whereas the β grain is extracted with the Zernike phase-contrast method. This is fundamentally attributable to the sensitivity difference between the two techniques. It is also associated with the above-mentioned characteristic contrast formation in the Zernike phase-contrast method. Only the first derivative of local density produces contrast in the case of the schlieren phase-contrast method. It has been reported that the chemical compositions differ between the primary α grain and the α plates in the α + β lamella region due to the segregation of solute atoms [21]. For example, it was reported by Chong et al. that the aluminium concentrations in a bimodal Ti-6Al-4V alloy annealed at 1153 K, 20 K lower than the heat treatment temperature in the present study, were approximately 8.5 and 6 mass % for the primary α grain and the α + β lamella regions, respectively [21]. It is reasonable to assume that the density of the α plates in the α + β lamella region is reduced due to such partitioning of the aluminium, providing a density value relatively close to that of the β grain; and this would appear to be the reason why there is no discernible contrast within the α + β lamella region with the schlieren phase-contrast method. In the case of the defocusing phase-contrast method, it is obvious that the edge enhancement effect is brought about mainly at the boundaries between the α and α + β lamella regions, and no substantial contrast is observed between the two regions. It can also be seen from Fig. 4 that there is a better signal-to-noise ratio in the Zernike phase-contrast method than in the schlieren phase-contrast method. This is probably due to the greater signal strength in the former method.

Another constraint in both the schlieren and defocusing phase-contrast methods is the remarkable artefact formation, as seen in Fig. 4. More than two different types of artefacts are seen in projected images, which might be reflected in reconstructed images in Figs. 4 (b) and (c). Some of these may originate in the imperfections in A-FZP, which are observed as thin ripple-like patterns in projection images, and secondary diffraction from the A-FZP, which appears as broad and bright arcs seen in projected images. The latter might correspond to wide blurred ring artefact dimly seen in Fig. 4 (b). In any case it may be concluded, even from this first comparative investigation, that more careful configuration, installation and alignment of the optics, and/or preparation of more precise optical devices, may be necessary to eliminate such artefacts in the schlieren phase-contrast method.

A useful balance between spatial resolution, contrast enhancement artefacts, and the simplicity of the experimental set-up must be found, depending on the microstructural features of the samples to be visualized and segmented. Overall, the Zernike phase-contrast method may be well suited for high-resolution and high-energy 3D imaging of metallic materials with a duplex microstructure with limited density difference.

4. Applications of the Zernike phase-contrast method for in-situ transformation observation of the duplex carbon steel：

Figure 5 shows virtual cross-sections of the duplex carbon steel under loading, which were visualized with the Zernike phase-contrast method at an X-ray energy of 20 keV. A 3D image obtained by employing the conventional projection-type XMT, which has a spatial resolution of 1.0 μm, is also shown as Fig. 5 (f) for reference purpose. Although the density difference between the two microstructures in the duplex carbon steel is as low as 0.7 %, much less than in the Ti-6Al-4V alloy (3.7 %), the metastable retained austenite is clearly visualized in the XNT images. There appear to be two different artefacts: the peripheral white fringe and the radial streaks in the XNT images. The former originates in the region of interest imaging [22]: the region of interest, here only 43 μm in diameter, is captured in the imaging-type XNT with respect to the entire specimen width of about 100 μm shown in Fig. 5 (f). The latter appears to be a kind of metal artefact [23] that is typically observed when regions with an extremely high or low grey scale are dispersed such that a metal particle with a high linear absorption coefficient is embedded in a polymer matrix with a low linear absorption coefficient. The reasonably low artefact degrees might enable image segmentation to quantitatively analyze the amount and morphologies of the dispersed grain. Roughly 22 vol. % of the metastable retained austenite was initially dispersed in the ferrite matrix (Fig. 5 (a)). It is seen that the retained austenite grain gradually shrinks over the loading history, and almost completely disappears at the applied nominal strain of 5.4 %. The metastable retained austenite is transformed into the martensite grain, which is, however, invisible with the present Zernike phase-contrast method.

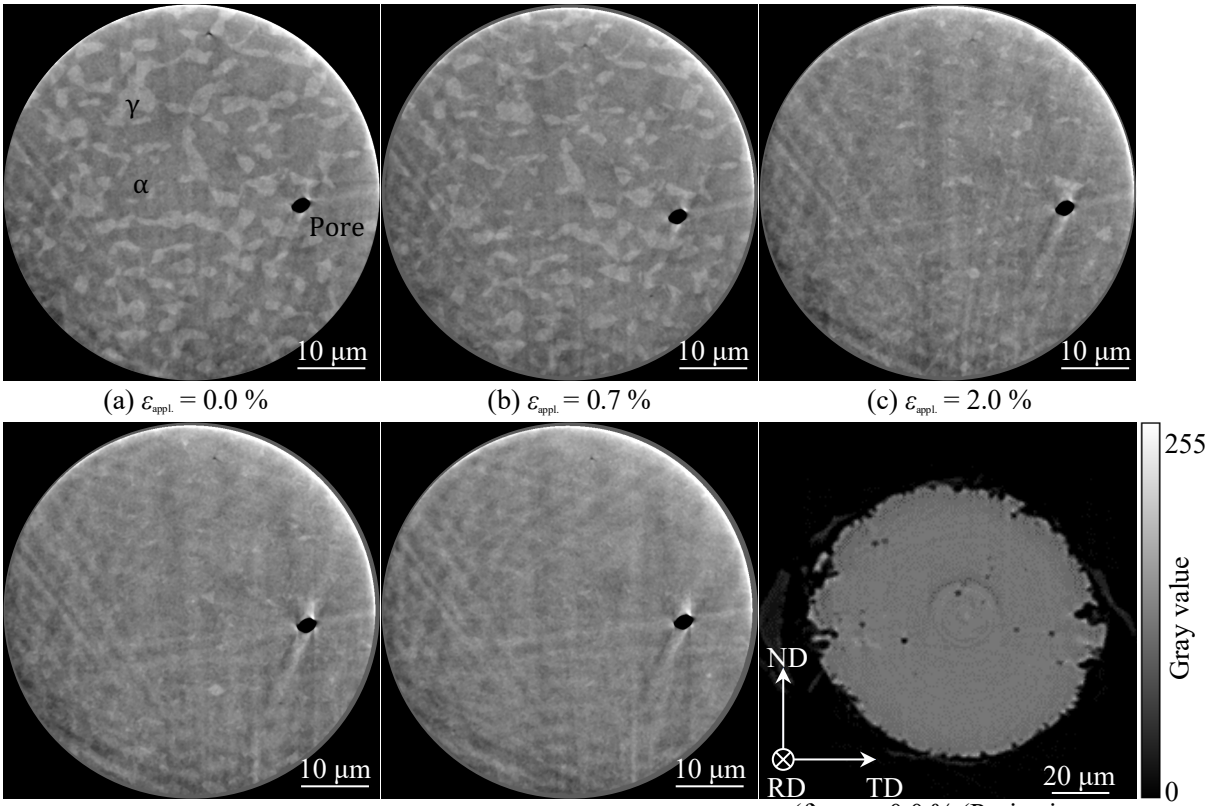

Fig. 5 In-situ transformation observation of the metastable retained austenite in the Fe-0.1C-5Mn-1Si duplex carbon steel under tensile loading. The same virtual cross-section is shown for evaluation purposes. The 3D images in (a) – (e) were captured using the Zernike phase-contrast method at an X-ray energy of 20 keV, whereas (f) was an absorption-contrast image captured using the projection-type XMT.

The local transformation behavior of retained austenite particles is illustrated in Fig. 6. Some of these particles remained intact in the early loading stage (highlighted with solid circles in Fig. 6 (a)), while a gradual transformation was seen in the case of others (highlighted with dotted circles in Fig. 6(b)). It has been well documented that the martensitic start temperature, Ms, is dependent on the carbon concentration, implying that the stability of an austenite grain is enhanced when the carbon concentration is high [24]. It has also been reported that carbon is locally enriched in the surface layer along ferrite / austenite boundaries [25], which is consistent with the tendency observed in Fig. 6, where the transformation starts locally from the inside of

each austenite grain. It is also interesting to note that the morphology of the retained austenite particles is associated with their stability, as shown in Fig. 7 (a), where circularity is defined as the degree of roundness of a given circle, representing the extent of irregularity in the shape of the retained austenite particles. It is inferred that irregularly shaped austenite grains cause elevation in the internal stress, thereby increasing the driving force for transformation. There appeared to be significant variation both in the loading step level at which transformation began, and in the duration of transformation, as summarized in Fig. 7 (b). This implies that factors affecting the transformation, such as the carbon concentration, vary grain by grain, both in nature and level.

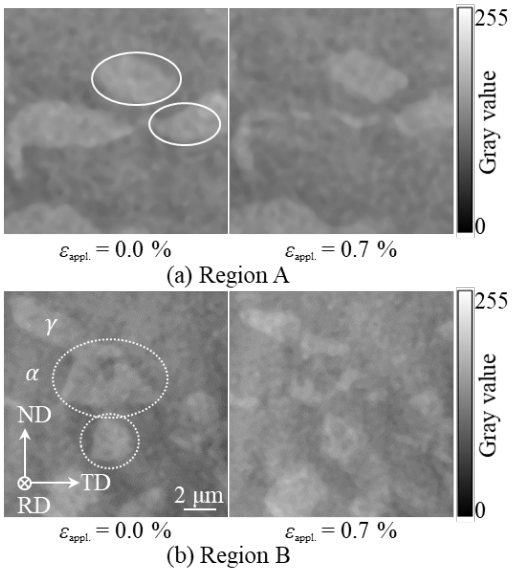

Fig. 6 Local transformation behavior of retained austenite particles, visualized using the same X-ray nanotomography data as in Fig. 5. In Region A, some of the retained austenite particles (highlighted with solid circles) remain completely intact in the early loading stage; whereas, the gradual transformation of retained austenite particles is seen in Region B (highlighted with dotted circles)

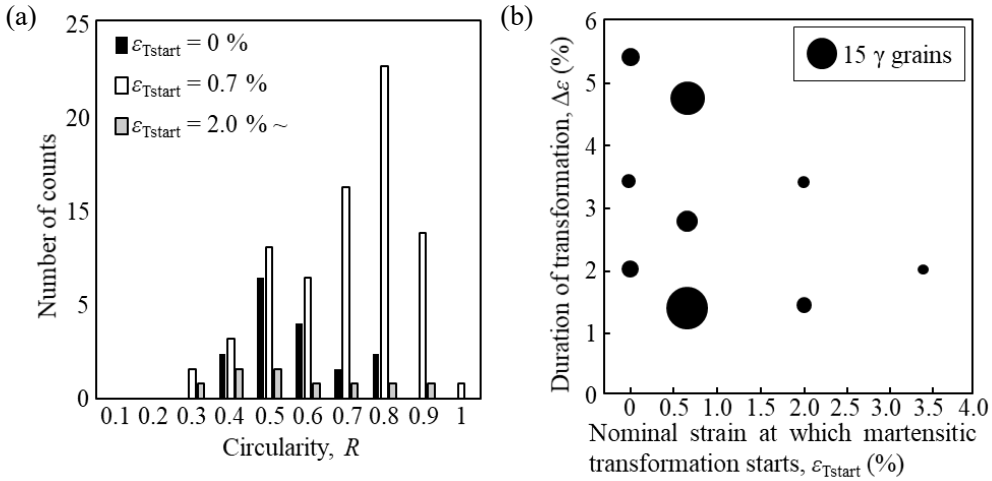

Fig. 7 (a) Histograms of the morphology of retained austenite particles in the Fe-0.1C-5Mn-1Si duplex carbon steel, which has been separated by strain levels at which the martensitic transformation starts, ε_{Tstart}. The horizontal axis expresses circularity, which is defined as the degree of roundness of a given circle. (b) Relationship between the strain level at which the martensitic transformation began, (ε_{Tstart}), and the duration of transformation expressed as the applied strain range ($\Delta\varepsilon$, in the Fe-0.1C-5Mn-1Si duplex carbon steel. Circle size denotes the number of retained austenite particles (larger circles represent larger particle numbers, as illustrated in the upper-right rectangle).

5. Summary：

Various attempts to achieve high-resolution, high-contrast 4D observation in structural metals have been reported in the recent literature. There appear, however, to be drawbacks to every method; among them, too

low an upper limit of X-ray energy for metallic samples, difficulty in the set-up for multi-scale observation, difficulty in applicability to 4D observation, etc. In the present study, the three types of high-resolution / high-energy phase-contrast XNT techniques were tested, and the spatial resolution, contrast between two microstructures with very limited density difference, and quantity and magnitude of artefacts were evaluated. The authors also focused on whether apodization Fresnel zone plates (A-FZPs), which have been developed for the purpose of improvement of imaging characteristics were useful for the high-resolution / high-energy phase-contrast XNT techniques, by utilizing the A-FZP's thicker inner zones, suitable for high X-ray energies. The available X-ray energy range for FZPs has long been limited to 10 keV or less due to the difficulty in their micro-fabrication. A-FZPs, however, are useful for the higher X-ray energies typically employed for 3D observation of bulky metallic samples.

The techniques tested were the imaging-type XNT combined with Zernike phase-contrast optics, the X-ray schlieren phase-contrast method, and the defocusing phase-contrast method. The Zernike phase-contrast method exhibited a combination of higher contrast and reduced artifact reconstruction. There appear to be compelling reasons for selecting the Zernike phase-contrast method as a technique for high-resolution and high-energy 3D imaging well suited to duplex metallic materials with very limited density difference. Even if the density difference between the two microstructures is less than 1 %, the Zernike phase-contrast method provides reasonably high contrast. It is however to be noted that according to the authors' experience, complex outer shape of a specimen tends to cause significant artefacts in the case of the Zernike phase-contrast method, thereby degrading image quality. This technique was then applied to in-situ 4D XNT observation of the transformation behavior of retained austenite in a duplex carbon steel, and the characteristic local transformation behavior of the retained austenite was successfully revealed. Finally, the imaging-type XNT combined with Zernike phase-contrast optics offers rapid switching to the projection-type XMT with a wider field of view, together with the desirable possibility of multi-modal techniques involving state-of-the-art diffraction-based techniques.

Acknowledgments：

One of the authors (HT) was also grateful for the support of the Grant-in-aid for Scientific Research from JSPS through Subject No. 17H01328, and the Light Metal Educational Foundation. The authors would also like to express their gratitude to wide-ranging supports from Nippon Steel Corp., especially those from Dr. Takeda of the same company.

References：

[1] A. Koch *et al*., *J. Opt. Soc. Am. A,* **15**, 1940 (1998).
[2] Y. Suzuki and H. Toda, in "Advanced Tomographic Methods in Materials Research and Engineering", Oxford University Press, 181 (2008).
[3] G. T. Herman, in "Fundamentals of Computerized Tomography: Image Reconstruction from Projections", Springer-Verlag, London, (2009).
[4] A. Momose, *Jap. J. Appl. Phys.*, **44**, 6355 (2005).
[5] S. K. Gill *et al*., *J. Electrochem. Soc.*, **166**, C3320 (2019).
[6] G. Requena *et al*., *Scripta Mater.*, **61**, 760 (2009).
[7] C. Landron *et al*., *Scripta Mater.*, **66**, 1077 (2012).
[8] B. M. Patterson *et al*., *Mater. Charact.*, **95**, 18 (2014).
[9] R. S. Bradley *et al*., *J. Microscopy*, **267**, 98 (2017).
[10] H. Toda *et al*., *Appl. Phys. Lett.*, **89**, 143112 (2006).
[11] A. Takeuchi *et al*., *J. Synchrotron Rad.*, **24**, 586 (2017).
[12] M. Born and E. Wolf, in "Principles of optics", pergamon Press Ltd., London, (1959).
[13] K. Goetz *et al*., *Sov. J. Quantum Electron*, **9**, 607 (1979).
[14] N. Watanabe *et al*., *10th Int. Conf. on X-ray Microscopy, AIP Conf. Proc.*, **1365**, 313 (2011).
[15] Y. Suzuki *et al*., *Proc. Int. Conf. SRI, AIP Conf. Proc*., **705**, 344 (2004).
[16] A. Takeuchi *et al*., *Microsc. Microanal.*, **24**, 106 (2018).
[17] G. T. Herman, in "Image reconstruction from projections: the fundamentals of computerised tomography", Academic Press, Orland, FL, (1980).
[18] Y. Kohmura *et al*., *Nuc. Instr. and Mthd. in Phys. Res. A*, **467**, 881 (2001).
[19] F. McBagonluni and W. O. Soboyejo, in "Advanced Structural Materials": Properties, Design Optimization, and Applications, in: W. O. Soboyejo and T. S. Srivatsan, (Eds.), CRC Press, Boca Raton, FL, 363 (2006).
[20] G. S. Kino and T. R. Corle, in "Confocal Scanning Optical Microscopy and Related Imaging Systems", Academic Press, San Diego, 229 (1996).
[21] Y. Chong, T. Bhattacharjee and N. Tsuji, *Mater. Sci. Engng. A*, **762**, 138077 (2019).

[22] B. Ohnesorge *et al*., *Med. Phys.*, **27**, 39 (2000).
[23] T. M. Buzug, in "Computed Tomography: From Photon Statistics to Modern Cone-Beam CT", Springer, Berlin, Germany, (2008).
[24] S. van der Zwaag *et al*., *ISIJ Int.*, **42**, 1565 (2002).
[25] H. S. Wang *et al*., *Mater. Sci. Engng. A*, **692**, 43 (2017).

(Received: March 12, 2021; Accepted: December 16, 2021; Published: February 28, 2022)